RSC Advances

PAPER

View Article Online
View Journal | View Issue

Cite this: *RSC Adv.*, 2026, **16**, 4937

Investigating catechol adsorption to the ZnO (10$\bar{1}$0) surface with and without an oxygen vacancies using the DFT-D2 method

Neha Kamal,[a] Arup Kumar De,[b] Anshu Shrivastava[a] and Indrajit Sinha *[a]

Functionalizing surfaces with different molecules can modulate their electronic properties and impart advantageous adsorption properties, which are crucial for various applications. For robust functionalization, chemisorption is required. Therefore, a molecular-level understanding of adsorption phenomena provides insight into the stability of the adsorbed molecule and its structure, crucial for designing catalysts, sensors, and other functional materials. This study employs detailed Density Functional Theory (DFT) calculations to investigate the adsorption behavior of catechol molecules on pristine ZnO and ZnOv (ZnO with oxygen-vacancy) (10$\bar{1}$0) surfaces. Bader charge analysis and electronic structure calculations provide insights into adsorption mechanisms. Both half- and fully protonated catechol configurations were chemically adsorbed on the ZnO surface. The bond length between O of catechol and Zn of the surface obtained in the most stable configuration (E_{ads} = 2.14 eV) was 1.95 Å, which is close to the bond length between Zn and O of the surface of ZnO. Additionally, a significant change in bond angle was also observed. This clearly shows the chemisorption phenomenon of catechol on the surface of ZnO. Nevertheless, catechol showed weaker chemisorption to the ZnOv surface only in a fully protonated state. In this case, the bond length between the O of catechol and the Zn of ZnO surface was found to be 2.31 Å. In both the surfaces (ZnO and ZnOv), Bader analysis reveals a charge transfer from the surface to the catechol molecule, leading to a reduction in the surface's overall positive charge. Electronic structure changes observed in the valence and conduction bands upon adsorption corroborate these findings. Experimental adsorption kinetics on ZnO nanoparticles further benchmark the DFT results, confirming chemisorption of catechol on the ZnO surface. This combined theoretical and experimental approach advances the understanding of molecule–ZnO surface interactions for the design of functional materials.

Received 8th December 2025
Accepted 30th December 2025

DOI: 10.1039/d5ra09496h

rsc.li/rsc-advances

1. Introduction

Oxidative degradation of phenolic compounds is a challenging process. Hence, adsorption is a typical wastewater treatment method for removing these chemicals from natural water. A widely used phenolic compound is catechol (1,2-dihydroxybenzene). Catechol is used to develop photographic (and fur) dyes.[1] It is also utilized as an antioxidant in the manufacture of rubber. Moreover, catechol is also crucial in the production of pharmaceutical compounds and cosmetics. Nevertheless, phenolic compounds like catechol are toxic and carcinogenic.[2,3] High industrial production and consumption of catechol also cause natural water pollution,[4] requiring remediation.

The removal of catechol by adsorption is one aspect of natural water remediation. However, in the case of chemisorption, the formation of a metal-oxide–catechol composite is a possibility. A composite exhibits different electronic and adsorption properties compared to either of its components. For instance, the unsuitable band gaps and adsorption properties of metal oxides, such as Fe_2O_3, TiO_2, Al_2O_3, SnO_2, and ZnO, encumber their performance in many applications. Functionalizing the surface with different molecules can tune the band gap and endow it with promising adsorption properties, making it suitable for various applications.[5] Thus, Jiang *et al.*[6] have tuned the band gap of germanane by varying the size of electron-donating and electron-withdrawing ligands. They found that ligands with electron-withdrawing groups decrease the band gap, whereas ligands with electron-donating groups increase the band gap.

Similarly, functionalizing the surface of large-bandgap ZnO, given its non-toxic and economical properties, could alter its electronic structure and enhance its adsorption activity. Hence, density functional theory (DFT) calculations have been

[a]*Department of Chemistry, Indian Institute of Technology (Banaras Hindu University), Varanasi 221005, India. E-mail: isinha.apc@iitbhu.ac.in*
[b]*Jyoti and Bhupat Mehta School of Health Sciences and Technology, Indian Institute of Technology Guwahati, Guwahati 781039, India*

employed to investigate the interaction of the Zn $(10\bar{1}0)$ surface with catechol. In this publication, the density of states (DOS) revealed the interaction of orbitals during the interaction between the two entities. A more in-depth investigation by Rangan *et al.*[7] of catechol adsorption on a single crystal of ZnO $(11\bar{2}0)$ revealed the possibility of a Type II composite formation between catechol and ZnO. These authors suggested the direct injection of photoexcited electrons from the catechol HOMO to the conduction band (CB) of ZnO. Calzolari *et al.*[8] investigated the adsorption of catechol on the ZnO $(10\bar{1}0)$ plane using plane-wave density functional theory (DFT) calculations. Optimization of catechol initially in two different orientations (parallel and perpendicular) relative to the ZnO surface gave the same structure. However, these authors did not conduct a detailed DFT study of this phenomenon. Especially, the authors did not consider the effect of adsorbate–adsorbent van der Waals interactions on the final adsorbed configuration. Furthermore, the system's complexity required spin-polarized calculations, which were also not performed by Calzolari *et al.*[8] The Bader charge calculations of these adsorbate configurations showed that fully protonated and half-protonated catechol weakly attract electrons from ZnO, whereas the fully deprotonated catechol donates electrons to the surface. In another study, Zhou *et al.*[9] investigated the adsorption of catechol on the ZnO surface using scanning tunneling microscopy along with *ab initio* calculations. They reported that the chemical adsorption of catechol to the ZnO surface can occur in three ways. In one case, the adsorbed catechol remains fully protonated. The second possibility is that the adsorbate (catechol) exists in a half-protonated form. The third way is that after adsorption, the catechol is fully deprotonated (Fig. S1).

Oxygen vacancies (OVs) in ZnO are an intrinsic defect.[10,11] OVs affect the electronic structure, and thereby the adsorption behaviour of the ZnO. Oxygen vacancies are considered important sites for many adsorbates. They can serve as a direct adsorption site, where an adsorbate can bind, and as an electron donor site, modulating local electronic properties.[12] There are no studies in the previous literature on the adsorption of catechol on ZnO with oxygen vacancies. Thus, in the present study, we investigate the adsorption of catechol on the nonpolar $(10\bar{1}0)$ plane of ZnO and ZnO having OVs (ZnOv) by appropriate plane wave DFT calculations. We perform spin-polarized catechol adsorption calculations, incorporating long-range dispersion correction using the DFT-D2 approach, to understand the effect of long-range electron correlations responsible for van der Waals forces.[13] Bader charges have also been calculated, allowing us to understand the charge distribution on the ZnO surface.[14] To the best of our knowledge, no such detailed analysis has been reported for catechol adsorption on the ZnO and ZnOv surfaces.

We have studied different orientations of catechol relative to the ZnO $(10\bar{1}0)$ surface using the Vienna *Ab initio* Simulation Package (VASP). The bond activation and change in bond angles of the adsorbed catechol in different conformations relative to the investigated ZnO plane were studied in detail. Previous investigators have neglected this aspect of catechol adsorption on ZnO. The density of states (DOS) reveals the orbitals responsible for altering the valence band (VB) and conduction band (CB) edges, thereby, the band gap. Simultaneously, experiments were also conducted to investigate catechol adsorption on ZnO. The prepared particles were extensively characterized by X-ray diffraction powder (XRD), Transmission Electron Microscope (TEM), Field Emission Scanning Electron Microscope (FE-SEM), FTIR spectroscopy, and X-ray photoelectron spectroscopy (XPS). The materials used for the synthesis of ZnO and the characterization techniques used for the detailed analysis are mentioned in Sections S1 and S2 of the SI.

The experimental investigations, along with the DFT calculation results, gave a deeper mechanistic insight into the adsorption of catechol on ZnO. A detailed adsorption mechanism study suggests that the obtained catechol-modified ZnO nanocomposite could have potential applications in sensors, optoelectronic devices, and catalysis.

2. Computational and experimental protocols

2.1. DFT calculation details

All theoretical calculations were carried out using the plane-wave density functional theory (DFT) within the Vienna *Ab initio* Simulation Package (VASP).[15,16] The models investigated in the present research were created using the MedeA VASP (2.22) software platform. The projector augmented wave (PAW) potential was used to define the interaction of core electrons, while the GGA-PBE (Generalized Gradient Approximation-Perdew–Burke–Ernzerhof) functional was employed to describe the exchange–correlation interaction.[17–19] The Hubbard potential ($U = 5.2$ eV) was introduced for Zn 3d electrons.[20] The convergence criteria were set to 10^{-5} eV for electronic energy and 0.02 eV Å^{-1} for the forces. Spin-polarized calculations, along with the Grimme (DFT-D2)[21] method, were employed to capture the van der Waals interactions between the adsorbate and the adsorbent.

2.2. Synthesis of ZnO nanoparticles

Appropriate aqueous solutions of Zn $(NO_3)_2 \cdot 6H_2O$ (4 mmol) and 0.4 M NaOH were prepared separately. The beaker containing $Zn(NO_3)_2 \cdot 6H_2O$ aqueous solution was placed on a magnetic stirrer, and the NaOH solution was added dropwise until the pH reached 12. This mixture was transferred into a Teflon-lined sealed stainless-steel autoclave and kept at 180 °C for 24 hours. The obtained precipitate was decanted and washed several times with distilled water and ethanol. Finally, the product obtained was dried at 50 °C for 24 hours to get a dried powder sample.

2.3. Adsorption of catechol on ZnO

Adsorption of catechol was measured by taking 20 ml of 600 ppm catechol solution (in distilled water) in a 25 ml conical flask. To the same flask, 50 μl of the prepared dispersion of ZnO nanoparticles (50 mg in 2 ml of distilled water) was added. It was subjected to bath sonication for 10 minutes. The mixture was agitated at 27 °C on a thermostatic shaker at 150 rpm. A

specific volume of the dispersion was separated using a syringe and passed through a 0.5 μm filter to remove the ZnO catalyst. The absorption spectrum of the supernatant was recorded in a UV-Vis spectrophotometer. This process was repeated at regular intervals to investigate the kinetics of catechol adsorption on ZnO.

3. Results and discussion

3.1. XRD

Fig. S2 shows the XRD of pure ZnO particles. Diffraction peaks are observed at 31.66°, 34.32°, 36.15°, 47.43°, 56.49°, 62.73°, 66.33°, 67.84°, 69.01°, 72.47°, 76.87°, 81.39°. These peaks match (101), (100), (002), (102), (110), (103), (200), (112), (201), (004), (202) and (104) planes of hexagonal wurtzite ZnO (JCPDS 75-1526) phase with primitive lattice having cell parameters $a =$ 3.220 Å and $c = 5.200$ Å. Fig. S3 shows the XRD before and after the adsorption of catechol on ZnO. No shifting in XRD peaks, as well as no extra peaks, were observed after the adsorption of catechol on ZnO.

3.2. TEM and FE-SEM

The TEM images of the prepared ZnO particles show that they have irregular shapes (Fig. S4a). Fig. S4b is the HR-TEM image of a typical ZnO particle. It exhibits lattice fringes with a *d*-spacing of ~0.25 nm (calculated using ImageJ software). This lattice spacing corresponds to the (002) crystallographic plane of the hexagonal wurtzite phase of ZnO (JCPDS no. 75-1526). FE-SEM was used to analyze the surface morphology and composition of the prepared particles. Fig. S5a and b show the microstructure images of the synthesized ZnO nanoparticles at different magnifications. The surface morphology was irregular in shape. Fig. S6 shows the particle size distribution of the ZnO powder sample. It has an average particle size of ~100 nm.

3.3. XPS

XPS analysis was carried out to obtain detailed information about the elemental composition and chemical states present on the sample surface. The full spectrum of XPS reveals the presence of Zn and O elements in the ZnO sample, as shown in Fig. 1a. Fig. 1b displays the Zn 2p spectrum, exhibiting characteristic peaks of Zn $2p_{3/2}$ and Zn $2p_{1/2}$ at binding energies of 1020.84 eV and 1043.93 eV, respectively.[22] This confirms the +2 oxidation of Zn. On the deconvolution of the XPS spectrum of O 1s, two peaks appear at 529.60 eV and 531.03 eV binding energies (Fig. 1c). The peak at 529.60 eV corresponds to the lattice oxygen (O^{2-} ion) bound to Zn, whereas the peak at 531.03 is attributed to the OH group present on the surface of ZnO nanoparticles.[23,24]

3.4. Fourier transform infrared (FT-IR) spectra

Fig. S7 compares the FT-IR spectra of catechol (as obtained), prepared ZnO, and ZnO particles with catechol adsorbed (denoted by ZnOcat). Table S1 provides detailed assignments of the characteristic FTIR peaks for catechol and ZnOcat. Fig. S7a presents the entire FTIR spectrum, spanning a wavenumber range of 400 cm^{-1} to 4000 cm^{-1}. The peaks labelled 19 and 20 represent two types of O–H stretching vibrations observed in catechol. Notably, peak 19 (Fig. S7a), assigned to the O–H stretching vibration of catechol involved in hydrogen bonding, disappears after adsorption. Nevertheless, this region becomes more intense in the ZnOcat FTIR. Peak 3, observed at 1637 cm^{-1}, corresponds to the bending vibration of water molecules adsorbed on the ZnO surface. The intensity of this peak increases after catechol adsorption to ZnO particles.

Fig. S7b displays only the 400 to 1000 cm^{-1} region of the FTIR spectra. It highlights peaks 1 and 2 at 439 and 490 cm^{-1} that appear in the ZnOcat FTIR. These are attributed to Zn–O stretching vibration.[25] A peak at 870 cm^{-1} that appeared before adsorption in ZnO, belonging to Zn–O[26] disappeared after adsorption of catechol on ZnO (ZnOcat). The catechol-specific FTIR peaks ranging from 448 to 935 cm^{-1} are characteristic of phenyl ring skeletal vibrations and phenyl C–H out-of-plane bending modes. However, these peaks are not visible in the ZnOcat FTIR.

Peaks 5 and 6 (in Fig. S7c), at 1040 and 1093 cm^{-1} in the FTIR of catechol, are assigned to phenyl C–H bending vibrations. These peaks are also observed in the FTIR of ZnOcat at slightly shifted wavenumbers of 1045 and 1089 cm^{-1}. Peaks labelled 7, 8, 9, and 14 (in Fig. S7c) are due to the bending vibrations of the C–OH groups of catechol. The ZnOcat FTIR of this region also displays these peaks. While peaks 7, 8, and 9 experience minor

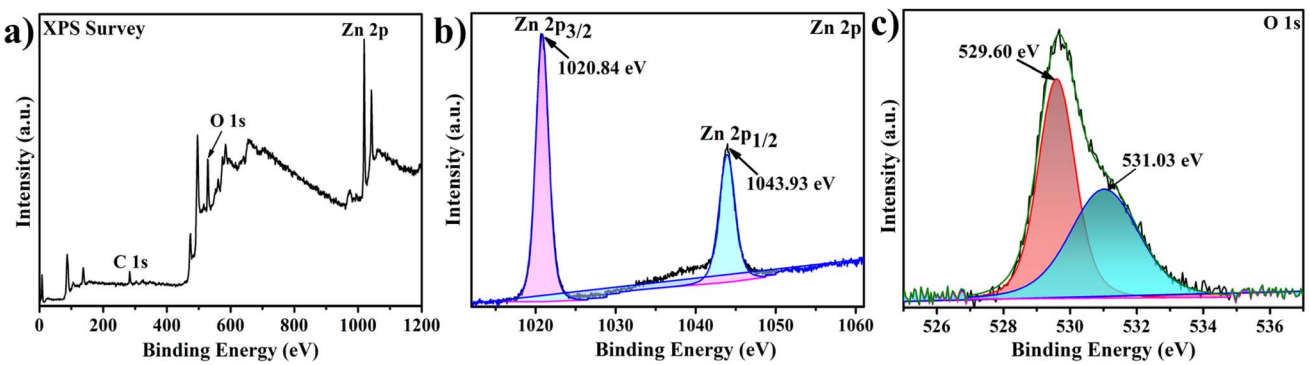

Fig. 1 (a) XPS survey spectra of ZnO nanoparticles, (b) Zn 2p, and (c) O 1s.

shifts, the position of peak 14 remains unaltered in the FTIR of ZnOcat. Similarly, peaks 10, 11 and 12, the C–OH stretching vibrations in the catechol FTIR, are also observed in the ZnOcat FTIR. However, the peaks in ZnOcat are broadened and shifted from the positions in catechol FTIR. A new peak observed at 1319 cm^{-1} could be due to the C–O bond of catechol attached to the Zn of the ZnO. Fig. S7d displays peaks 15 to 18. These are attributed to the stretching vibrations of C–C and C=C bonds. Among these, only peak 15 at 1598 cm^{-1} appeared in the ZnOcat FTIR. In general, the appearance of the above catechol FTIR peaks in the FTIR of ZnOcat at slightly shifted positions demonstrates the adsorption of catechol to ZnO.[27]

3.5. Adsorption kinetics

Fig. S8 shows the kinetics graph plotted between adsorption capacity (q_t) at time t *versus* time (t) for the adsorption of catechol over the ZnO surface. The obtained adsorption kinetics data have been fitted to the pseudo-first-order (PFO) and pseudo-second-order (PSO) adsorption kinetics models. These adsorption kinetics equations are phenomenological. Nevertheless, PFO kinetics generally indicate a physisorption mechanism, whereas PSO typically suggests adsorption through chemical bonding.[28] Eqn (1) and (2) give the PFO and PSO equations, respectively.

$$q_t = q_e(1 - \exp(k_1 t)) \quad (1)$$

$$q_t = \frac{k_2 q_e^2 t}{1 + k_2 q_e t}, \quad (2)$$

In eqn (1) and (2), q_t represents the adsorption capacity (in mg g^{-1}) at time t, whereas q_e is the adsorption capacity (in mg g^{-1}) at equilibrium, k_1 and k_2 are the rate constants for PFO and PSO, respectively. The fit parameters in Table S2 show that the catechol adsorption kinetics data fit to the PSO model are much better than those to the PFO kinetic model, implying catechol has been chemisorbed on ZnO nanoparticles.[29,30]

4. DFT calculations

In this work, a primitive unit cell of ZnO (COD#2107059)[31] was multiplied to obtain a 3 × 3 × 3 supercell. This supercell was optimized using a 5 × 5 × 5 k-point mesh and an energy cut off of 500 eV (Fig. S9 and S10). The initial lattice parameters of ZnO were 'a' = 3.2417 Å and 'c' = 5.1876 Å. The calculated lattice constant after optimization was found to be 'a' = 3.2049 Å and 'c' = 5.170 Å. A surface of the $(10\bar{1}0)$ plane was created from this optimized supercell, comprising a total of six (9.61 Å × 15.51 Å) layers. A vacuum of 15 Å was added to prevent slab–slab interaction and provide sufficient space for the adsorbate. The bottom four layers were fixed, and the upper two layers were relaxed. This slab was optimized with 4 × 1 × 3 k-mesh points and an energy cutoff of 500 eV. The same k-mesh and energy cutoff were used for optimizing the entire slab with the catechol molecule. The band gap obtained for the ZnO supercell was 1.52 eV. It reduced to 1.099 eV for the ZnO $(10\bar{1}0)$ surface. This reduction in the band gap of the slab is attributed to the breaking of chemical bonds at the surface and the relaxation of the two upper layers, which affects the electronic structure of the slab.[32,33] Fig. 2a shows the optimized structure of ZnO $(10\bar{1}0)$ surface.

For modelling the ZnOv surface, the O21 oxygen was removed from the optimized slab of the ZnO surface. This structure was optimized using the same parameters as mentioned above (Fig. 2a and b). Fig. 3 shows Zn21 forming new bonds with Zn25 and Zn43. The Zn21–Zn43 and Zn21–Zn25 distances, before O21 removal, were ~2.97 Å. After optimization of the ZnOv surface, the Zn21–Zn43 and Zn21–Zn25 distances decreased to 2.48 Å, near the typical dizinc complex bond distances.[34] In contrast, the Zn43–Zn25 distance changed from 3.20 Å to 2.84 Å, after optimization of the ZnOv surface.

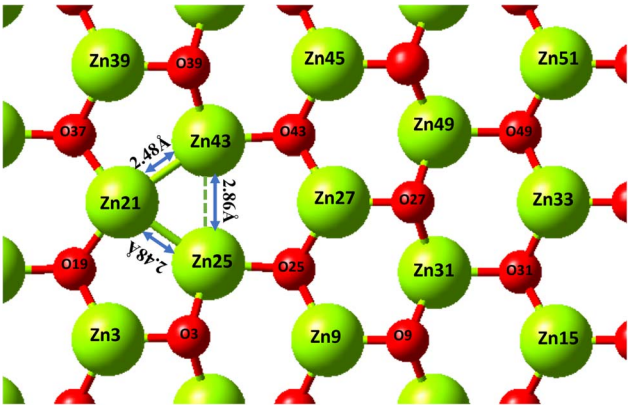

Fig. 3 Top view of optimized structure of ZnOv $(10\bar{1}0)$ surface.

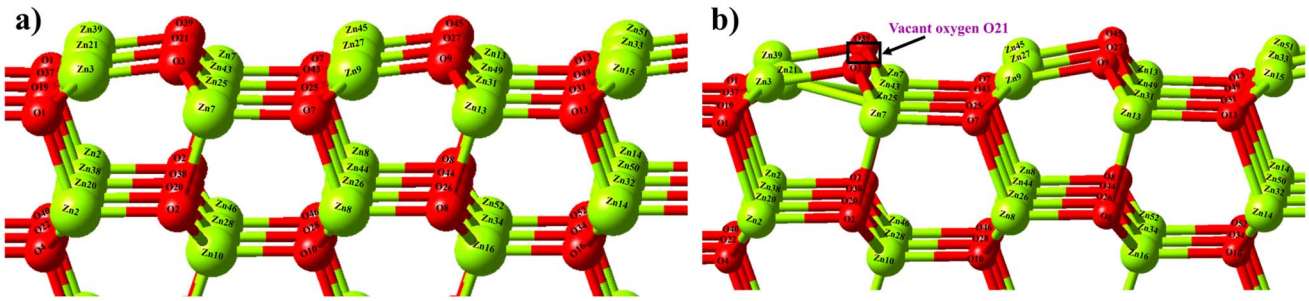

Fig. 2 Optimized structure of (a) pure ZnO and (b) ZnOv $(10\bar{1}0)$ surface.

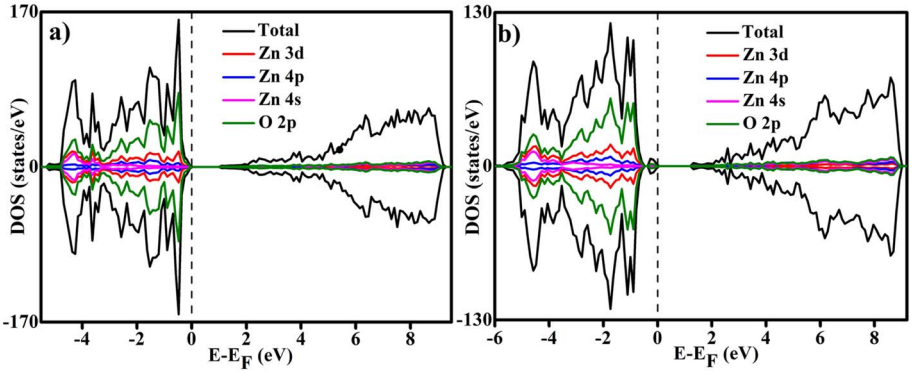

Fig. 4 The TDOS and PDOS of the (10$\bar{1}$0) surfaces of the (a) ZnO and the (b) ZnOv systems.

Fig. 4a and b show the total density of the states (TDOS) and the partial density of states (PDOS) of the (10$\bar{1}$0) surfaces of ZnO and ZnOv systems. Fig. S11a and b display the (10$\bar{1}$0) surface PDOS of ZnO and ZnOv systems. It revealed that the VB is mainly composed of O 2p orbitals, along with the amalgamation of Zn 3d, 4p, and 4s orbitals. The conduction band (CB) also exhibits very low-intensity peaks of Zn 3d, 4s, 4p, and O 2p. However, in the case of ZnOv (10$\bar{1}$0) surface (Fig. 4b), a new state is observed near the Fermi level. This new state ranges from −0.26 to −0.05 eV near the VB maximum. This state arises because of oxygen vacancy unpaired electrons on the surface.[35]

4.1. Adsorption of catechol on the (10$\bar{1}$0) surface of ZnO

For the optimization of Catechol, the catechol structure was modeled in MedeA VASP. It was placed in a cubic cell of 20 Å. The *k*-point used for its optimization was 1 × 1 × 1 and an energy cutoff of 500 eV. Gaussian smearing with a width of 0.05 eV was used, and the same potential and functionals were utilized as mentioned in Section 2.

Fig. 5 shows the optimized structure of catechol. Table S3 presents a comparison of various bond lengths in the catechol molecule obtained from the present work with those reported in previous experimental studies.[36,37] Meanwhile, the DFT-calculated bond lengths and bond angles in catechol, reported by Mian *et al.*,[38] Gerhards,[39] and E. Obeid *et al.*,[40] are also compared in Table S3. The bond lengths of C–C, C–O, and C–H match the experimentally known values (Table S3). The bond angle of C2–O56–H6 and C2–C1–O55 were approximately the same as the experimental value. The adsorption of the catechol molecule was studied on both pure ZnO and ZnOv (10$\bar{1}$0) surfaces. The catechol molecule was placed on the surface of ZnO (10$\bar{1}$0) in four different orientations. One was parallel to the surface, another was perpendicular, and the other two were tilted (Fig. S12). The adsorption energy was calculated by using eqn (3).

$$E_{\text{adsorption}} = E_{(\text{surface+adsorbate})} - [E_{(\text{surface})} + E_{(\text{adsorbate})}] \quad (3)$$

In eqn (3), $E_{(\text{surface+adsorbate})}$ is the total energy of the slab (ZnO or ZnOv) and the catechol molecule, $E_{(\text{surface})}$ is the energy of the surface (ZnO or ZnOv) only, and, $E_{(\text{adsorbate})}$ is the energy of the catechol molecule. A negative value of $E_{\text{adsorption}}$ reveals that the system has released the energy due to adsorption (exothermic) and is favourable. On the contrary, if $E_{\text{adsorption}}$ is positive it means adsorption requires energy and is endothermic.

All four configurations of catechol demonstrate sufficiently negative adsorption energies on the ZnO surface for them to be characterized as chemisorption[41,42] (Table 1). Among the four orientations, configurations 'pr' and 'pl' demonstrate the lowest (most negative) adsorption energies of −2.14 eV and −1.96 eV. We first discuss the particulars of catechol adsorption on ZnO in the 'pr' configuration. In this configuration, the molecule was initially oriented perpendicular to the surface (with only the O and H atoms lying near the surface). After optimization, the catechol adsorbed to the ZnO (10$\bar{1}$0) surface through a half-protonated configuration (Fig. 6). Both oxygen atoms of

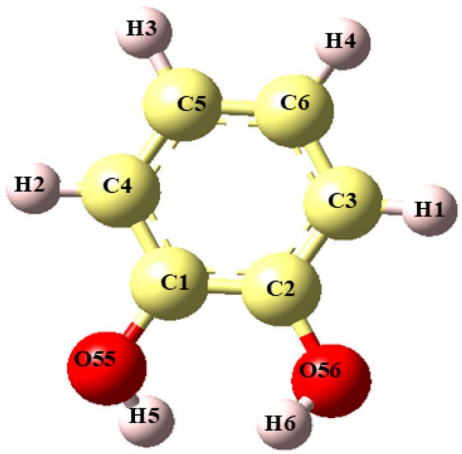

Fig. 5 Optimized structure of catechol.

Table 1 Adsorption energies of catechol on ZnO (10$\bar{1}$0) surface

Configuration	E_{ads} (eV)
pr	−2.14
t1	−1.41
t2	−1.32
pl	−1.96

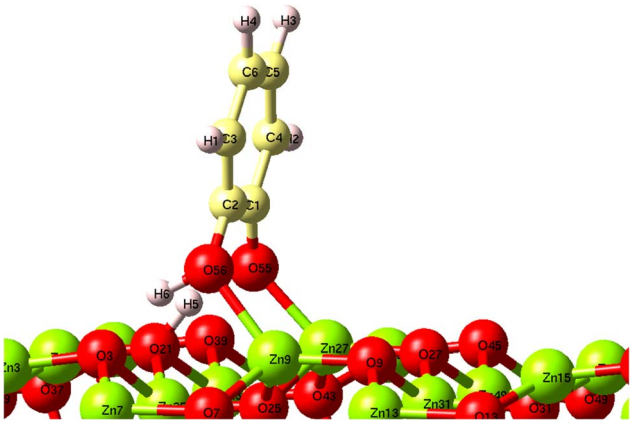

Fig. 6 Optimized structure of configuration "pr" of catechol adsorbed on ZnO surface. The green, red, yellow, and light pink balls represent zinc, oxygen, carbon, and hydrogen atoms, respectively.

catechol got attached to two different (but adjacent) Zn atoms (Zn9 and Zn27) of the ZnO (10$\bar{1}$0) surface. The H5 (hydrogen) dissociated from the O55 (oxygen) of catechol (Fig. 6) and got attached to the O21 (oxygen) of the zinc oxide surface. Nevertheless, the O56–H6 bond remains unaffected. Note the bond length of Zn27–O55 is 1.96 Å, very near to the Zn–O bond length (1.95 Å) in fixed layers of ZnO. In contrast to this, the Zn9–O56 bond length is 2.05 Å. The bond length of the new bond formed between O21 of ZnO and H5 of catechol O–H is 1.07 Å, longer than the typical O–H bond length of catechol, *i.e.*, 0.97 Å. Table S4 lists all bond lengths in configuration 'pr' of catechol adsorption on the (10$\bar{1}$0) ZnO system. It is observed that the bond lengths of Zn9 with O9, O7, and O25, and Zn27 with O25, O27, and O43 increased. The C2–C1–O55 bond angle changed from 120.12° to 122.61°, and the C2–C1–O56 bond angle underwent a larger transformation from 114.82° to 121.60° (Table S4). Table S5 compares the data obtained in Table S4 with those from previous DFT calculation studies on the adsorption of catechol on different metal oxide (and metal oxide-based composite) surfaces.

As mentioned earlier, configuration 'pl' showed an adsorption energy of −1.96 eV. Configuration 'pl' initially placed the catechol molecule ∼2.5 Å above the (10$\bar{1}$0) ZnO surface in a parallel orientation. Fig. S12a displays the DFT optimized structure of catechol adsorbed on the (10$\bar{1}$0) ZnO surface from this initial (parallel) configuration. The optimized structure reveals that the catechol molecule remains fully protonated after adsorption to the (10$\bar{1}$0) ZnO surface. Only one oxygen (O) of catechol got linked to the 'Zn' of ZnO (Fig. S12a). Fig. S12b and c show the DFT optimized structures obtained when the catechol molecule was placed in two different tilted orientations (configurations t1 and t2). In both cases, catechol adsorbs to the (10$\bar{1}$0) ZnO surface in half-protonated configurations, and only one oxygen interacts with a Zn of the ZnO surface.

Here, it is critical to point out that Calzolari *et al.*[8] have reported both 'pr' and 'pl' type orientations resulted in half-protonated catechol adsorption to the (10$\bar{1}$0) ZnO surface. Furthermore, Zhou *et al.*[9] have reported from their STM (Scanning Tunneling Microscopy) experiments that catechol has been found to adsorb to the (10$\bar{1}$0) ZnO surface in half protonated, fully protonated (FP), and fully deprotonated (FD) forms. However, the adsorption energies and probabilities for the fully protonated and deprotonated configurations were much lower than those in the half-protonated configuration. In this respect, the observations from the present DFT calculations indicate that the catechol adsorbs to (10$\bar{1}$0) ZnO surface in the half-protonated configuration agrees with Zhou *et al.* This observation also implies that the catechol molecule possibly approaches the (10$\bar{1}$0) ZnO surface in a perpendicular fashion.

4.2. Adsorption of catechol on ZnOv (10$\bar{1}$0) surface

We examined catechol adsorption on the ZnOv (10$\bar{1}$0) surface in the perpendicular configuration. The latter entails that the hydroxyl groups of the catechol molecule are oriented towards the ZnO (10$\bar{1}$0) surface. Fig. 7 shows the optimized geometry of catechol adsorbed to the ZnOv surface. This configuration is denoted by the abbreviation 'ovpr'. It occurs in a fully protonated configuration. The 'ovpr' adsorption configuration exhibited an adsorption energy of −1.21 eV, typical for chemisorption. The latter contrasts with the half-protonated adsorbed catechol configuration observed for the 'pr' system (Fig. 6). Furthermore, a new bond 2.31 Å in length is formed between Zn27 and O54 (Fig. 7). While the bond length is greater than the typical Zn–O bond length, it is much smaller than the sum of van der Waals radii of the concerned atoms, implying a weaker chemisorption-type interaction.[43] Table S6 shows the change in the lengths of different bonds and bond angles in the 'ovpr' ZnOv–catechol adsorbed configuration.

In the present ZnOv case, catechol binds to the ZnO surface through a single Z27–O54 bond. We can refer to this as a monodentate binding geometry. The latter contrasts with the bidentate[44,45] catechol binding geometry exhibited on the ZnO surface in the absence of oxygen vacancies. The reason behind forming a monodentate bond between O54 of catechol and Zn27 of the (10$\bar{1}$0) ZnOv surface could be stabilized due to the formation of intramolecular O54–H5···O55–H6 hydrogen bonds.[46] Since O21 is absent, this hydrogen bond remains

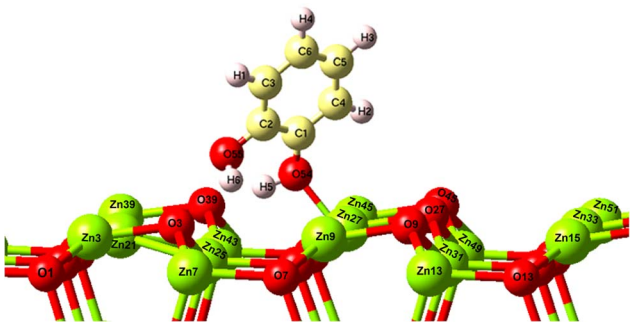

Fig. 7 The 'ovpr' configuration showing adsorption of catechol on the ZnOv surface. Given the removal of one oxygen to model the oxygen vacancy, the rest of the oxygens were renumbered. Thus, the earlier O55 and O56 changed to O54 and O55, respectively.

intact. Consequently, O55 does not bond with Zn9 as previously mentioned in the adsorption of catechol on (10$\bar{1}$0) ZnO surface.

4.3. Bader charges

4.3.1. Bader charges of the 'pr' and 'ovpr' configuration. Table S7 shows the Bader charges calculated on each participating atom of the (10$\bar{1}$0) ZnO and the ZnOv surfaces. Table S8 gives the Bader charges on different atoms after the adsorption of catechol to the ZnO (10$\bar{1}$0) surface in the 'pr' and the ZnOv surface in the 'ovpr' configurations. The initial charge on the ZnO surface was 0.108*e*. The charge on the ZnO surface increased to 0.146*e* ('pr' configuration) after catechol adsorption. Correspondingly, the charge on catechol after adsorption to ZnO changed from 0.0608 to −0.0132*e*. Overall, electron transfer occurred from the ZnO surface to catechol after adsorption.

The O21 oxygen was removed to create the ZnOv surface. This decreased the positive charge on Zn21 from 1.162*e* (before oxygen vacancy) to 0.611*e* (after oxygen vacancy). Before adsorption, the overall charge on the ZnOv (10$\bar{1}$0) surface was 0.105*e*. After catechol adsorption, the overall surface charge of ZnOv changed to 0.158*e*. At the same time, the charge on catechol after adsorption changed from 0.0608*e* to −0.0304*e*. This implies electron transfer from the ZnOv surface to catechol on the adsorption of the latter to the former. Furthermore, the magnitude of electron transfer is greater than that observed for catechol adsorption on the ZnO surface. The ZnOv surface has oxygen vacancy electrons. Hence, there is more electron transfer from the ZnOv surface to the adsorbed catechol.

4.4. Electronic properties

4.4.1. Electronic properties of configuration "pr". This subsection presents the density of states (DOS) results for ZnO surface and the change therein due to catechol adsorption. Fig. 8 presents the total density of states (TDOS) of the ZnO surface before and after catechol adsorption, highlighting the modifications in both the valence band (VB) and conduction band (CB). Notably, both bands exhibit a downward shift in energy upon adsorption, indicative of a pronounced interaction between the catechol adsorbate and the ZnO surface. This interaction arises from orbital hybridization between the electronic states of ZnO and catechol.

Fig. S13 compares the projected density of states (PDOS) of the orbitals of the atoms that constitute ZnO and catechol. The figure contains PDOS of orbitals before and after the adsorption of catechol on ZnO. Following adsorption, there is a marked increase in the intensity of the O 2p PDOS peak near the Fermi level within the ZnO–catechol system, indicating charge transfer and the formation of a chemical bond. Similarly, the C 2p PDOS exhibits enhanced features after catechol adsorption. Additionally, the emergence of a new state near the Fermi energy in the H 1s PDOS of catechol (Fig. S13), absent in the isolated catechol molecule, underscores the participation of hydrogen 1s orbitals in the adsorbate–substrate interaction.[47]

Overall, comparison of Fig. S13 with the ZnO TDOS prior to adsorption (Fig. 8a) reveals the incorporation of catechol-derived C 2p and O 2p states within the valence band region of the combined ZnO–catechol TDOS (Fig. 8b and S13). The presence of these orbitals confirms the electronic coupling between catechol and the ZnO surface. Moreover, the formation of shallow occupied states near the Fermi level provides strong evidence for chemisorption rather than physisorption.[48]

4.4.2. Electronic properties of configuration "ovpr". Fig. 9 compares the TDOS of the ZnOv (10$\bar{1}$0) surface before and after adsorption of catechol. There are only small changes in the TDOS of ZnO after catechol adsorption. A slight shifting was observed in both the VB minima and the CB maxima positions. Fig. S14 displays the PDOS of orbitals of elements constituting the ZnOv and catechol before and after the adsorption of catechol on ZnOv. There are some changes in the PDOS of the orbitals of elements, which are observed before and after

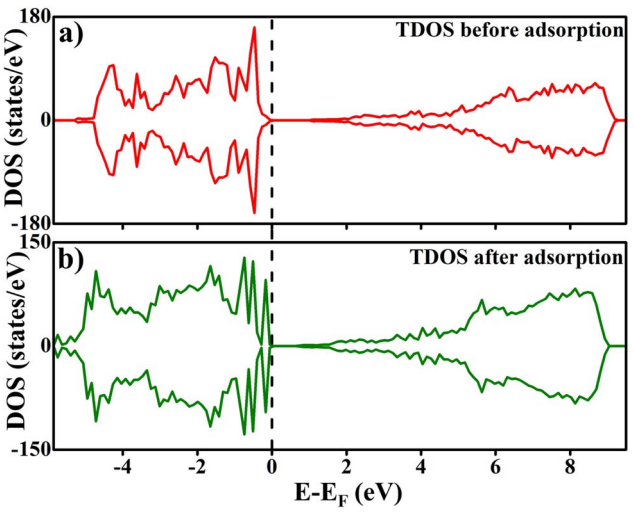

Fig. 8 TDOS of the 'pr' configuration, (a) before and (b) after catechol adsorption on ZnO.

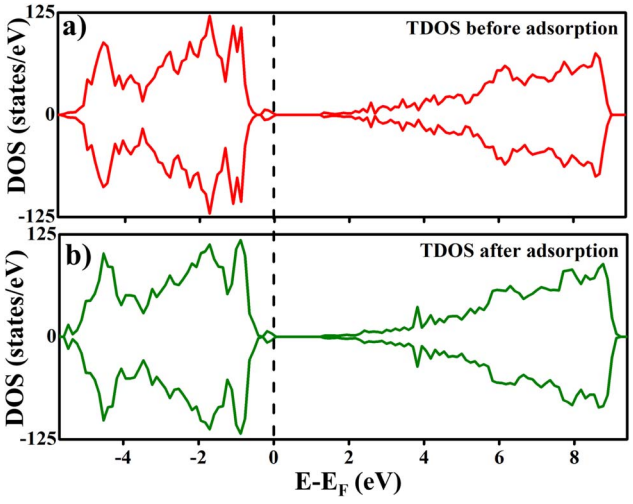

Fig. 9 A comparison of the S1 TDOS of ZnOv (10$\bar{1}$0) surface with the TDOS of the 'ovpr' configuration, (a) before adsorption, and (b) after adsorption of catechol adsorbed on ZnOv.

catechol adsorption. Thus, some new peaks can be observed in the PDOS of C 2s, C 2p, and O 2p orbitals after its adsorption to ZnOv. In contrast, the individual PDOS of the Zn 4s, 4p, and 3d orbitals does not exhibit any new peaks due to catechol adsorption. However, these PDOS plots do exhibit a change in the intensity of individual peaks. The change in the PDOS of O 2p (of oxygen in ZnOv) before and after catechol adsorption is similar. In view of the above, it may be said that the catechol molecule interacts with the ZnOv surface through weak chemisorption. This observation is commensurate with the earlier observation of the energy of adsorption of catechol on ZnO surface with oxygen vacancy.

5. Conclusions

Detailed DFT calculation-based and experimental investigations have been carried out to understand the adsorption mechanism of catechol on ZnO and ZnOv $(10\bar{1}0)$ non-polar surfaces. Specific DFT investigations have been employed to elucidate the impact of varying initial catechol configurations on their adsorption to the $(10\bar{1}0)$ ZnO surface. Two configurations demonstrated significant adsorption energies in the strong chemisorption range. The case in which catechol was perpendicular to the ZnO surface showed higher adsorption energy than the other configuration. The catechol in the perpendicular (adsorbate–adsorbent) configuration resulted in a half-protonated adsorbed configuration, while the initial parallel configuration led to a fully protonated adsorbed configuration. This shows the chemisorption behaviour of adsorption of catechol on the surface of ZnO. Furthermore, the kinetic studies of catechol adsorption on ZnO reveal that the process follows pseudo-second-order kinetics, thereby supporting the chemisorption mechanism. In contrast to this, adsorption of catechol to ZnOv $(10\bar{1}0)$ surface took place through a slightly tilted (but nearly perpendicular) fully protonated catechol configuration. In both cases, charge transfer occurred from the ZnO (or ZnOv) surface to the catechol molecule. The lower adsorption energy and little electronic structure change after catechol adsorption to the ZnOv surface indicated weak chemisorption or physisorption. The physisorption phenomenon offers an advantage, as catechol can be readily desorbed, enabling adsorbent regeneration and reuse.

Author contributions

Neha Kamal: writing – original draft, visualization, investigation, formal analysis, data curation. Arup Kumar De: formal analysis. Anshu Shrivastava: formal analysis and data curation. Indrajit Sinha: writing – review & editing, validation, supervision, software, resources, methodology, formal analysis, conceptualization.

Conflicts of interest

There are no conflicts to declare.

Data availability

The additional data supporting this article have been included as part of the supplementary information (SI). Supplementary information: instrumental details for material characterization, materials used in the synthesis of the sample, DFT structure of catechol, XRD Analysis, TEM and SEM images, FTIR analysis, experimental kinetics data, DFT calculation of supercell and surface, optimized configurations, comparison of the DFT calculated parameters, Bader charges, comparison of PDOS of all the orbitals. See DOI: https://doi.org/10.1039/d5ra09496h.

Acknowledgements

The author (Neha Kamal) acknowledges CSIR for providing a senior research fellowship 09/1217(0073)/2019-EMR-I. The authors further acknowledge CIF-IITBHU for offering several facilities for material characterization. The computational resources provided by the Centre for Computing and Information Service (CCIS) at IIT(BHU) are acknowledged.

References

1 S. Jiao, J. Tang, X. Li, Y. Zhai and M. Li, *Microchem. J.*, 2025, **211**, 113065, DOI: 10.1016/j.microc.2025.113065.
2 A. A. Ensafi, M. Amini and B. Rezaei, *Biosens. Bioelectron.*, 2014, **53**, 43–50, DOI: 10.1016/j.bios.2013.09.030.
3 A. Padmanaban, G. Murugadoss, N. Venkatesh, S. Hazra, M. Rajesh Kumar, R. Tamilselvi and P. Sakthivel, *J. Environ. Chem. Eng.*, 2021, **9**, 105976, DOI: 10.1016/j.jece.2021.105976.
4 M. Benjelloun, N. El Messaoudi, Y. Miyah, J. Georgin, D. S. P. Franco, E. Šehović, Y. Dehmani and S. Knani, *J. Water Process Eng.*, 2025, **76**, 108115, DOI: 10.1016/j.jwpe.2025.108115.
5 S. Sakib, F. Bakhshandeh, S. Saha, L. Soleymani and I. Zhitomirsky, *Sol. RRL*, 2021, **5**, 2100512, DOI: 10.1002/solr.202100512.
6 S. Jiang, K. Krymowski, T. Asel, M. Q. Arguilla, N. D. Cultrara, E. Yanchenko, X. Yang, L. J. Brillson, W. Windl and J. E. Goldberger, *Chem. Mater.*, 2016, **28**, 8071–8077, DOI: 10.1021/acs.chemmater.6b04309.
7 S. Rangan, J. P. Theisen, E. Bersch and R. A. Bartynski, *Appl. Surf. Sci.*, 2010, **256**, 4829–4833, DOI: 10.1016/j.apsusc.2010.01.111.
8 A. Calzolari, A. Ruini and A. Catellani, *J. Am. Chem. Soc.*, 2011, **133**, 5893–5899, DOI: 10.1021/ja1101008.
9 D. Zhou, Y. Wang, Y. Sun, J. Zhang, D. Wang, Z. Li and X. Shao, *Appl. Surf. Sci.*, 2023, **610**, 155504, DOI: 10.1016/j.apsusc.2022.155504.
10 Y. Imanaka, X. Chao-Nan, K. Harada, T. Mizoguchi, H. Takeda, K. Kato, H. Nagata and T. Kiguchi, *J. Ceram. Soc. Jpn.*, 2017, **125**(6), 445–448, DOI: 10.2109/jcersj2.125.P6-1.
11 N. Singh, U. Kumar, N. Jatav and I. Sinha, *Langmuir*, 2024, **40**, 8450–8462, DOI: 10.1021/acs.langmuir.3c04039.

12 A. Dey, *Mater. Sci. Eng., B*, 2018, **229**, 206–217, DOI: 10.1016/j.mseb.2017.12.036.
13 S. Grimme, *J. Comput. Chem.*, 2006, **27**, 1787–1799, DOI: 10.1002/jcc.20495.
14 M. Dukić, V. Lazić, S. Stavrić, M. Milenković and D. N. Sredojević, *ChemistrySelect*, 2025, **10**, 02227, DOI: 10.1002/slct.202502227.
15 G. Kresse and J. Furthmü, *Phys. Rev. B: Condens. Matter Mater. Phys.*, 1996, **54**, 1169, DOI: 10.1103/PhysRevB.54.11169.
16 G. Kresse and J. Furthmiiller, *Comput. Mater. Sci.*, 1996, **6**, 15–50, DOI: 10.1016/0927-0256(96)00008-0.
17 G. Kresse and D. Joubert, *Phys. Rev. B: Condens. Matter Mater. Phys.*, 1999, **59**, 1758, DOI: 10.1103/PhysRevB.59.1758.
18 J. P. Perdew, J. A. Chevary, S. H. Vosko, K. A. Jackson, M. R. Pederson, D. J. Singh and C. Fiolhais, *Phys. Rev. B: Condens. Matter Mater. Phys.*, 1993, **48**, 4978, DOI: 10.1103/PhysRevB.46.6671.
19 J. P. Perdew, K. Burke and M. Ernzerhof, *Phys. Rev. Lett.*, 1997, **78**, 1396, DOI: 10.1103/PhysRevLett.77.3865.
20 S. L. Dudarev, G. A. Botton, S. Y. Savrasov, C. J. Humphreys and A. P. Sutton, *Phys. Rev. B: Condens. Matter Mater. Phys.*, 1998, **57**, 1505, DOI: 10.1103/PhysRevB.57.1505.
21 S. Grimme, *J. Comput. Chem.*, 2006, **27**, 1787–1799, DOI: 10.1002/jcc.20495.
22 R. Al-Gaashani, S. Radiman, A. R. Daud, N. Tabet and Y. Al-Douri, *Ceram. Int.*, 2013, **39**, 2283–2292, DOI: 10.1016/j.ceramint.2012.08.075.
23 J. Lee, J. Chung and S. Lim, *Phys. E*, 2010, **42**, 2143–2146, DOI: 10.1016/j.physe.2010.04.013.
24 J. Das, S. K. Pradhan, D. R. Sahu, D. K. Mishra, S. N. Sarangi, B. B. Nayak, S. Verma and B. K. Roul, *Phys. B*, 2010, **405**, 2492–2497, DOI: 10.1016/j.physb.2010.03.020.
25 L. G. da Trindade, G. B. Minervino, A. B. Trench, M. H. Carvalho, M. Assis, M. S. Li, A. J. A. de Oliveira, E. C. Pereira, T. M. Mazzo and E. Longo, *Ceram. Int.*, 2018, **44**, 10393–10401, DOI: 10.1016/j.ceramint.2018.03.053.
26 M. Hjiri, S. Algessair, R. Dhahri, H. B. Albargi, N. Ben Mansour, A. A. Assadi and G. Neri, *RSC Adv.*, 2024, **14**, 5001–5011, DOI: 10.1039/d3ra08181h.
27 I. M. Dugandžić, D. J. Jovanović, L. T. Mančić, N. Zheng, S. P. Ahrenkiel, O. B. Milošević, Z. V. Šaponjić and J. M. Nedeljković, *J. Nanopart. Res.*, 2012, **14**, 1157, DOI: 10.1007/s11051-012-1157-1.
28 T. B. da Costa, M. G. C. da Silva and M. G. A. Vieira, *J. Rare Earths*, 2020, **38**, 339–355, DOI: 10.1016/j.jre.2019.06.001.
29 A. Shrivastava, J. Kuntail, U. Kumar and I. Sinha, *J. Mol. Liq.*, 2023, **389**, 122392, DOI: 10.1016/j.molliq.2023.122932.
30 M. K. Abugazleh, B. Rougeau and H. Ali, *J. Environ. Chem. Eng.*, 2020, **8**, 104180, DOI: 10.1016/j.jece.2020.104180.
31 S. Graulis, D. Chateigner, R. T. Downs, A. F. T. Yokochi, M. Quirós, L. Lutterotti, E. Manakova, J. Butkus, P. Moeck and A. Le Bail, *J. Appl. Crystallogr.*, 2009, **42**, 726–729, DOI: 10.1107/S0021889809016690.
32 A. Stashans, *Int. J. Nanotechnol.*, 2004, **1**, 399–430, DOI: 10.1504/IJNT.2004.005977.
33 N. Martsinovich, D. R. Jones and A. Troisi, *J. Phys. Chem. C*, 2010, **114**, 22659–22670, DOI: 10.1021/jp109756g.
34 R. Ayala, E. Carmona and A. Galindo, *Inorg. Chim. Acta*, 2018, **470**, 197–205, DOI: 10.1016/j.ica.2017.06.008.
35 L. Dong, R. Jia, B. Xin, B. Peng and Y. Zhang, *Sci. Rep.*, 2017, **7**, 40160, DOI: 10.1038/srep40160.
36 C. J. Brown, *Acta Crystallogr.*, 1966, **21**, 170, DOI: 10.1107/S0365110X66002482.
37 O. I. Alajrawy and A. M. EeSee, *J. Mol. Liq.*, 2025, **434**, 128056, DOI: 10.1016/j.molliq.2025.128056.
38 S. A. Mian, L. C. Saha, J. Jang, L. Wang, X. Gao and S. Nagase, *J. Phys. Chem. C*, 2010, **114**, 20793–20800, DOI: 10.1021/jp1070538.
39 M. Gerhards, W. Perl, S. Schumm, U. Henrichs, C. Jacoby and K. Kleinermanns, *J. Chem. Phys.*, 1996, **104**, 9362–9375, DOI: 10.1063/1.471682.
40 E. Obeid, N. Murshid, J. Arayro and M. Abu-Samha, *Phys. Scr.*, 2023, **98**, 125416, DOI: 10.1088/1402-4896/ad0e53.
41 M. A. Mahmoud, *Beni-Suef Univ. J. Basic Appl. Sci.*, 2015, **4**, 142–149, DOI: 10.1016/j.bjbas.2015.05.008.
42 M. P. Mudoi, P. Sharma and A. S. Khichi, *J. Pet. Sci. Eng.*, 2022, **217**, 110897, DOI: 10.1016/j.petrol.2022.110897.
43 A. Kokalj, *Corros. Sci.*, 2022, **196**, 109939, DOI: 10.1016/j.corsci.2021.109939.
44 V. Lazić and J. M. Nedeljković, *Catalysts*, 2024, **14**, 810, DOI: 10.3390/catal14110810.
45 R. Ponnusamy, R. Venkatesan, A. Gangan, R. Samal, B. Chakraborty, D. J. Late and C. S. Rout, *Appl. Surf. Sci.*, 2019, **495**, 143588, DOI: 10.1016/j.apsusc.2019.143588.
46 T. D. Manh, M. Van Bay and N. M. Thong, *ChemistrySelect*, 2025, **10**, 05581, DOI: 10.1002/slct.202405581.
47 Q. Qin, H. Qin, K. Li, R. Tan, X. Liu and L. Li, *RSC Adv.*, 2020, **10**, 2104–2112, DOI: 10.1039/c9ra06665a.
48 H. Cheng, H. He, Z. Zhang, K. Xiao, Y. Liu, X. Kang and X. Li, *Sep. Purif. Technol.*, 2022, **303**, 122282, DOI: 10.1016/j.seppur.2022.122282.